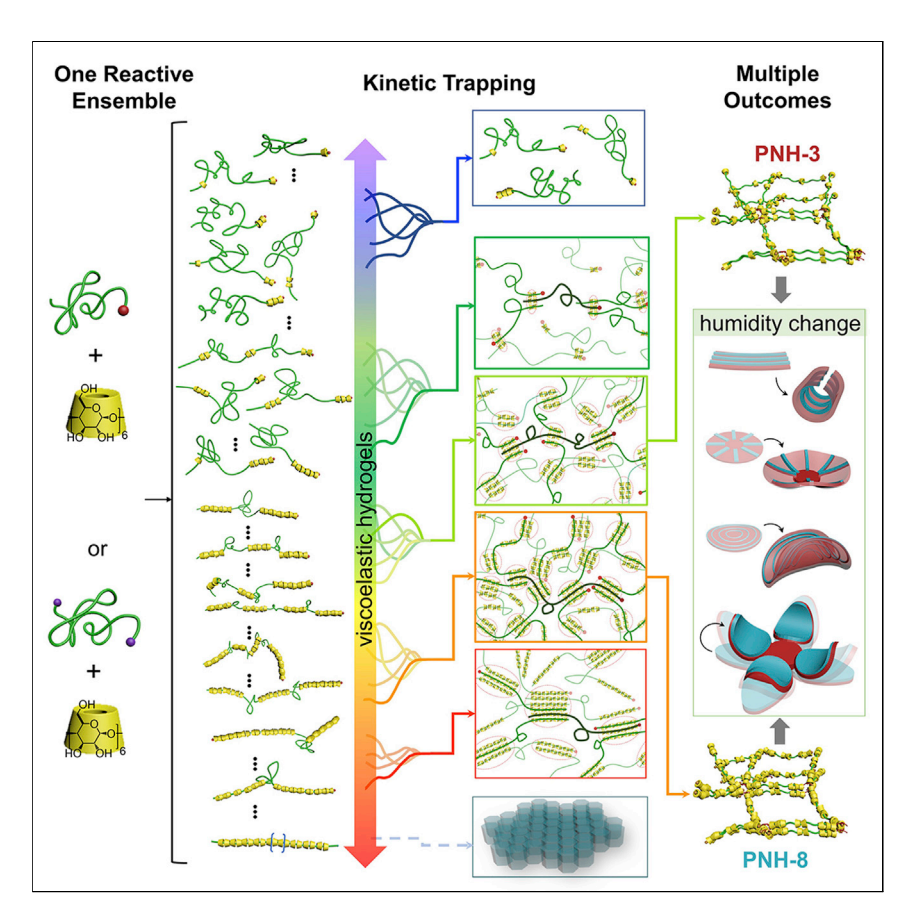




### **Article**

# Kinetic trapping of 3D-printable cyclodextrinbased poly(pseudo)rotaxane networks



A concerted kinetic trapping method is demonstrated to capture different  $\alpha\text{-cyclodextrins}$  and polyethylene glycols-based polypseudorotaxane network hydrogels. Varying the 3D printing temperatures, one hydrogel was diverged to two polyrotaxane networks and fabricated as a moisture-responsive actuator.

Qianming Lin, Longyu Li, Miao Tang, ..., Lingyi Zou, Kohzo Ito, Chenfeng Ke

kohzo@edu.k.u-to-kyo.ac.jp (K.I.) chenfeng.ke@dartmouth.edu (C.K.)

#### Highlights

The kinetic formation of polypseudorotaxane was navigated synthetically

A series of physically crosslinked networks were kinetically trapped

One reactive ink was diverged into two networks by varied-temperature-3D printing

Packing models of polypseudorotaxanes in the solidstate was corrected





Chem



#### **Article**

# Kinetic trapping of 3D-printable cyclodextrin-based poly(pseudo)rotaxane networks

Qianming Lin,<sup>1,4</sup> Longyu Li,<sup>1,4</sup> Miao Tang,<sup>1,4</sup> Shuntaro Uenuma,<sup>2,4</sup> Jayanta Samanta,<sup>1</sup> Shangda Li,<sup>1</sup> Xuanfeng Jiang,<sup>3</sup> Lingyi Zou,<sup>1</sup> Kohzo Ito,<sup>2,\*</sup> and Chenfeng Ke<sup>1,5,\*</sup>

#### **SUMMARY**

Synthetically trapping kinetically varied (super)structures of molecular assemblies and amplifying them to the macroscale is a promising, yet challenging, approach for the advancement of meta-stable materials. Here, we demonstrated a concerted kinetic trapping design to timely resolve a set of transient polypseudorotaxanes in solution and harness a crop of them via micro-crystallization. By installing stopper or speed bump moieties on the polymer axles, meta-stable polypseudorotaxanes with segmented cyclodextrin blocks were hierarchically amplified into crystalline networks of different crosslinking densities at mesoscale and viscoelastic hydrogels with 3D-printability in bulk. We demonstrated simultaneous 3D-printing of two polypseudorotaxane networks from one reactive ensemble and their conversion to heterogeneous polyrotaxane monoliths. Spatially programming the macroscale shapes of these heterogeneous polyrotaxanes enabled the construction of moisture-responsive actuators, in which the shape morphing originated from the different numbers of cyclodextrins interlocked in these polyrotaxane networks.

#### **INTRODUCTION**

Supramolecular assemblies, formed under thermodynamic control, have been advanced as a plethora of architectures with high order<sup>1</sup> and high complexity,<sup>2</sup> as well as stimuli-responsive behaviors.<sup>3,4</sup> Meta-stable materials<sup>5–7</sup> and dissipative systems,<sup>8</sup> formed under kinetic control, often demonstrate superior properties compared with their thermodynamic counterparts due to the differences in energy between their kinetically trapped and stable states. For example, meta-stable metal alloys, perovskites, organic crystals, and organogels show high strength and ductility,<sup>5</sup> efficient solar-electric conversion,<sup>6</sup> high porosity,<sup>7</sup> and photo-switchability,<sup>9–12</sup> respectively, giving rise to their kinetically trapped structures and morphologies.

Kinetically varied structures and superstructures, however, are often short-lived, and they converge to their stable states rapidly under thermodynamic control. Conventional approaches to trap these transient kinetic variants for the synthesis of metastable materials usually involve large physical changes such as rapid cooling and ultrahigh-pressure treatment. <sup>13,14</sup> Delicate control of the physical variation is critical in this process, due to the co-existence of multiple kinetic paths. <sup>15,16</sup> In contrast, synthetically modulating the kinetic process to harness the high-energy states <sup>17</sup> offers better selectivity in trapping the desired meta-stable species. To date, diverting the formation of molecular assemblies chemically into kinetic paths was largely

#### The bigger picture

Meta-stable polymers hold promise for the development of next-generation intelligent materials due to their positive free energy compared with the stable states. However, conventional development of meta-stable materials heavily relies on preparation methods, i.e., rapid cooling, high-pressure treatment, and controlled diffusion. The lack of understanding and control of these kinetic processes across the nano-to-macroscale challenges the rational synthesis of metastable materials. Herein, we demonstrated a synethetic approach to access polypseudorotaxanes' metastable states at the molecular level, navigated their crystallization at mesoscale, effectively amplified their structural features to the macroscale, and spatially programmed them as 3D-printed actuators. Future refinements of the axle polymer and speed bump design will expand the metastable states' control and network architectures. We envision fabricating 3D architectures with complex soft robotic motions through this approach.





achieved in solution through the modulation of strong non-covalent interactions. <sup>8,15,16</sup> Design principles to direct the kinetic assembly process across the nano-to-macroscale remain largely heuristic.

In the exploration of the rational design of meta-stable poly(pseudo)rotaxane materials, <sup>18</sup> we seek to divert the formation and crystallization of  $\alpha$ -cyclodextrin ( $\alpha$ -CD) and polyethylene glycol (PEG)-based polypseudorotaxanes away from the thermodynamic path (Figure 1A). By installing stopper or threading "speed bumps" 18-20 on the PEG chain end(s), the kinetic energy barriers 14 for the solution-phase polypseudorotaxanes assembly were raised (Figure 1B). A spectrum of polypseudorotaxanes with segmented α-CD blocks (Figure 2) was kinetically resolved and microcrystallized, following new kinetic crystallization paths with lower energy barriers (Figure 1B). We discovered that the solution-phase kinetic assembly and micro-crystallization of polypseudorotaxanes is a concerted process, affording meta-stable products as physically crosslinked hydrogels with suitable viscoelasticity for direct-ink-write<sup>21</sup> (DIW) 3D-printing. By diverging the same reactive ensemble of PEG<sub>4k</sub>-Nor<sub>2</sub> and  $\alpha$ -CD simultaneously into two kinetically trapped polypseudorotaxane hydrogels at two temperatures, we obtained 3D-printed heterogeneous polypseudorotaxane hydrogels with spatially configured shapes and compositions. We permanently fixed these meta-stable polypseudorotaxane networks through postprinting covalent crosslinking, and converted them as polyrotaxane networks. As a result of the different numbers of mechanically interlocked  $\alpha$ -CDs in each polyrotaxane network, they demonstrated different responsiveness to humidity changes. We demonstrated that, by varying the macroscale 3D-printing designs, the obtained heterogeneous polyrotaxane monoliths exhibited pre-programmed moistureresponsive actuations.

#### **RESULTS**

#### Molecular design considerations

When  $\alpha$ -CDs are threaded onto a short-to-medium chain PEG (smPEG,  $M_n < 6$  kDa), the smPEG axle is covered by a tube of consecutively hydrogen-bonded  $\alpha$ -CDs, <sup>22–24</sup> forming crystalline polypseudorotaxane precipitates with constant ethylene glycol (EG): $\alpha$ -CD molar ratios. <sup>25</sup> These investigations by others <sup>25</sup> and us <sup>24</sup> suggest that the threading and translocation energy barriers of  $\alpha$ -CDs onto smPEGs are small in solution (Figure 1A), but the energy barrier for polypseudorotaxane crystallization is relatively large (rate determining step). Any kinetic variant of polypseudorotaxane in solution was converged to the stable form before crystallization, thus preventing the isolation of kinetically trapped polypseudorotaxanes.

To access these kinetic variants chemically, the energy barrier for the formation of polypseudorotaxane in solution needs to be raised relative to the energy barrier of micro-crystallization (Figure 1B). We designed two types of energy barriers (Figure 2)— (1) by installing a stopper onto one end of the PEG, the translocation distances of  $\alpha$ -CDs are elongated compared with bare PEG. The coiled PEG axle acts as a dynamic energy barrier to slow down the translocation of  $\alpha$ -CDs. (2) By attaching sterically demanding "speed bumps" onto both ends of the PEG, the threading of  $\alpha$ -CDs onto the PEG axle is decelerated. Experimentally, we chose adamantylester (-Ad) as the stopper and norbonylester (-Nor) as the speed bump ( $\sim$ 4.7 Å) for  $\alpha$ -CDs, respectively. Smaller end groups, including hydroxyl (-OH), acetylester (-Ac), and benzoylester (-Bz), were also synthesized as  $\alpha$ -MeO- $\omega$ -R-PEGs (Figure 1C), which were employed as reference axles.

https://doi.org/10.1016/j.chempr.2021.06.004

<sup>&</sup>lt;sup>1</sup>Department of Chemistry, Dartmouth College, Hanover, NH 03755, USA

<sup>&</sup>lt;sup>2</sup>Department of Advanced Materials Science, The University of Tokyo, 5-1-5 Kashiwanoba, Kashiwa, Chiba 277-8561, Japan

<sup>&</sup>lt;sup>3</sup>Key Laboratory of Green Preparation and Application for Functional Materials, Ministry of Education, School of Materials and Engineering, Hubei University, Wuhan 430062, China

<sup>&</sup>lt;sup>4</sup>These authors contributed equally

<sup>&</sup>lt;sup>5</sup>Lead contact

<sup>\*</sup>Correspondence: kohzo@edu.k.u-to-kyo.ac.jp (K.I.), chenfeng.ke@dartmouth.edu (C.K.)





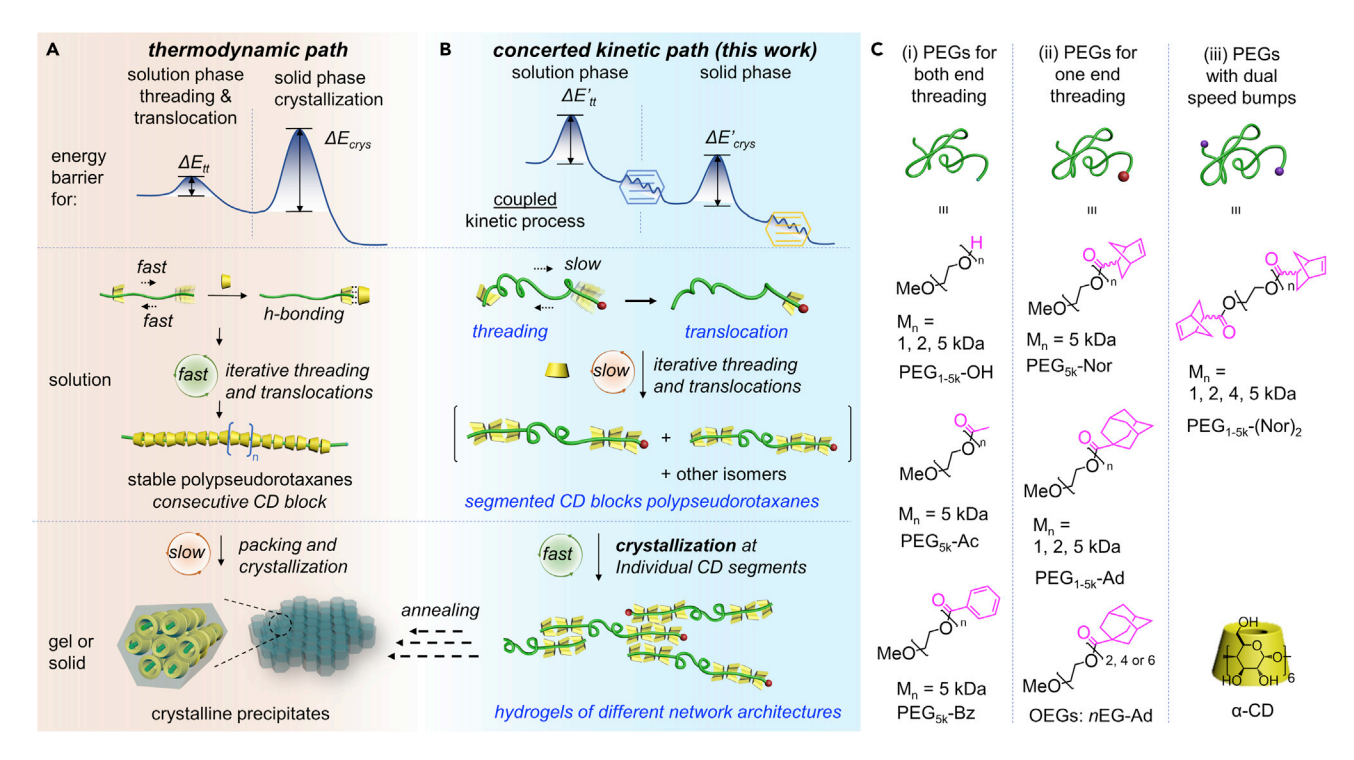


Figure 1. A comparison between the conventional crystalline polypseudorotaxane formation and the concerted kinetic formation of polypseudorotaxane networks via threading-and-crystallization path

(A and B) Energy barriers and graphical representations of the conventional polypseudorotaxanes formation under thermodynamic control (A) and the concerted kinetic formation of meta-stable polypseudorotaxane networks (B). The decelerated threading and translocation of  $\alpha$ -CDs on the PEG axle stabilized the otherwise transient polypseudorotaxanes with segmented  $\alpha$ -CD blocks, which enabled a new path for kinetic micro-crystallization. (C) PEGs and oligoethylene glycols (nEG-Ad) employed for the formation of  $\alpha$ -CD-based polypseudorotaxanes.

## Kinetic investigations of meta-stable polypseudorotaxane networks formation

In a PEG<sub>5k</sub>-OH (1 mM) and  $\alpha$ -CD (50 mM) mixture (20°C),  $\alpha$ -CDs rapidly threaded onto PEG<sub>5k</sub>-OH and crystallized as white suspensions. The transmittance<sup>29</sup> of the reaction decreased rapidly over time (Figure 3A) due to the increased light scattering (550 nm) of the fast-forming crystalline precipitates. Similarly, the transmittance of reactions of PEG<sub>5k</sub>-Ac/ $\alpha$ -CD and PEG<sub>5k</sub>-Bz/ $\alpha$ -CD also decreased quickly upon mixing. In parallel, crystalline PEG<sub>5k</sub>-OH/ $\alpha$ -CD polypseudorotaxanes formed at different times were collected for <sup>1</sup>H NMR analysis (Figure 3B). The number of  $\alpha$ -CDs threaded onto PEG<sub>5k</sub>-OH was measured to be independent of the reaction time at a constant of 41  $\pm$  1  $\alpha$ -CDs per PEG. These observations are consistent with previous reports,<sup>29</sup> indicating the formation of these crystalline polypseudorotaxanes underwent the thermodynamic path.

When PEG<sub>5k</sub>-Ad (1 mM) was mixed with  $\alpha$ -CD (50 mM) at 20°C, the transmittance of the reaction did not change for a long period ( $\sim$  100 min, Figure 3C), suggesting that the rate of polypseudorotaxane formation is significantly reduced compared with PEG<sub>5k</sub>-OH/ $\alpha$ -CD ( $\sim$  15 min) in solution. Time-dependent <sup>1</sup>H NMR experiments revealed that the polypseudorotaxane consists of a constant 42  $\pm$  2  $\alpha$ -CDs per PEG<sub>5k</sub>-Ad (Figure 3B). In the temperature-dependent polypseudorotaxane formation experiments (Figure 3D), the reaction of PEG<sub>5k</sub>-Ad and  $\alpha$ -CD showed "V"-shaped transmittance changes at 25°C and 30°C. This two-stage polypseudorotaxanes precipitation was also confirmed in the time-dependent <sup>1</sup>H NMR experiment (Figure S10). These experiments suggested that, over a period of time, the





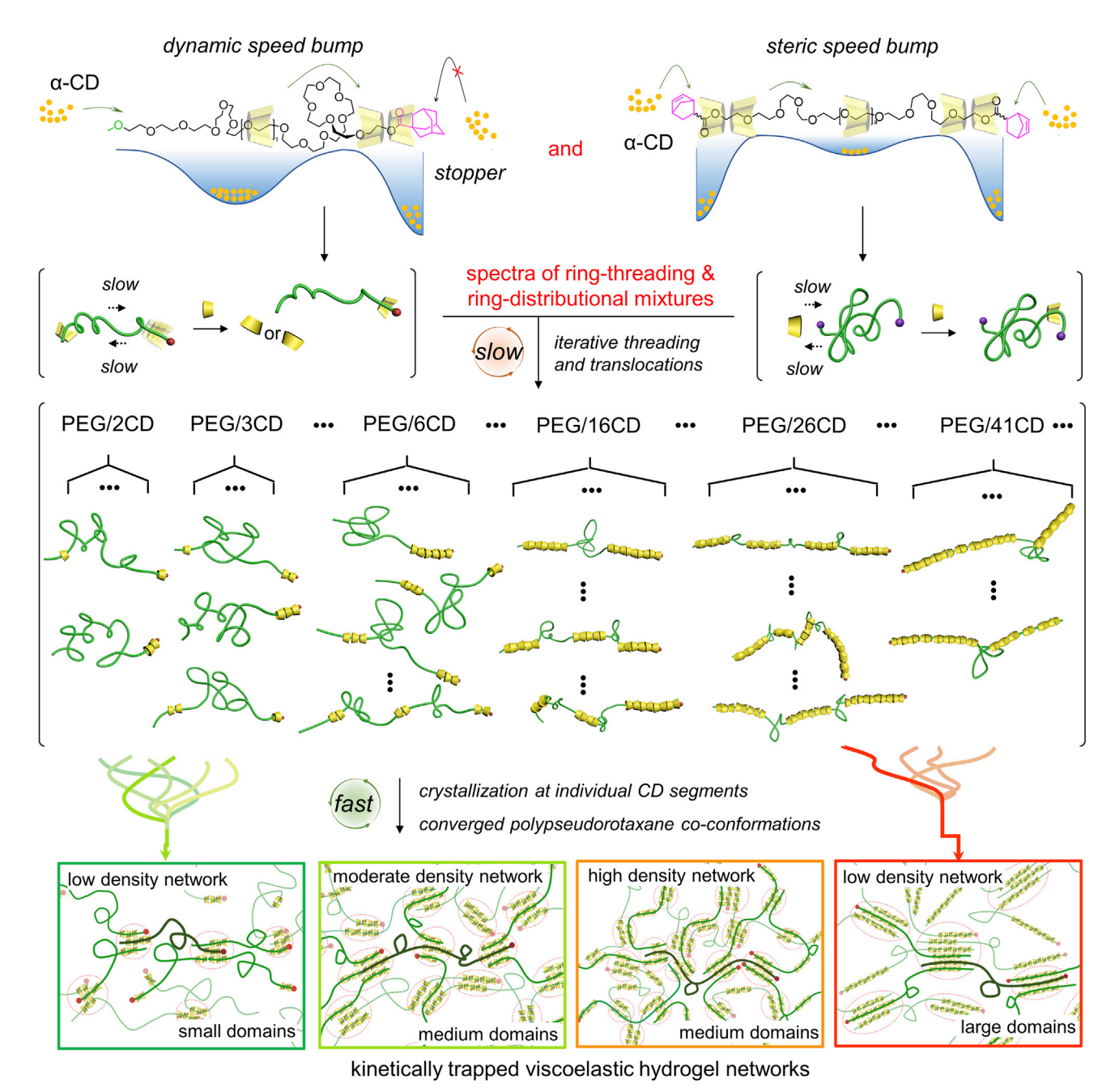


Figure 2. Kinetic trapping of meta-stable polypseudorotaxane networks of different crosslinking densities

Adamantylester and norbonylester end group(s) were installed on PEG axles, creating kinetic barriers to diverge the threading and translocation of  $\alpha$ -CDs, resolving a spectrum of polypseudorotaxanes in solution. These polypseudorotaxanes were trapped by kinetic micro-crystallization to afford physically crosslinked crystalline networks of various densities.

accumulated PEG $_{5k}$ -Ad/ $\alpha$ -CD polypseudorotaxanes in solution were not sufficient to allow for continuous crystallization. The rate of the PEG $_{5k}$ -Ad-based polypseudorotaxanes formation in solution and the rate of their crystallization became much more comparable.

The differences in crystallization kinetics between PEG<sub>5k</sub>-OH/ $\alpha$ -CD and PEG<sub>5k</sub>-Ad/ $\alpha$ -CD polypseudorotaxanes were investigated by temperature-dependent





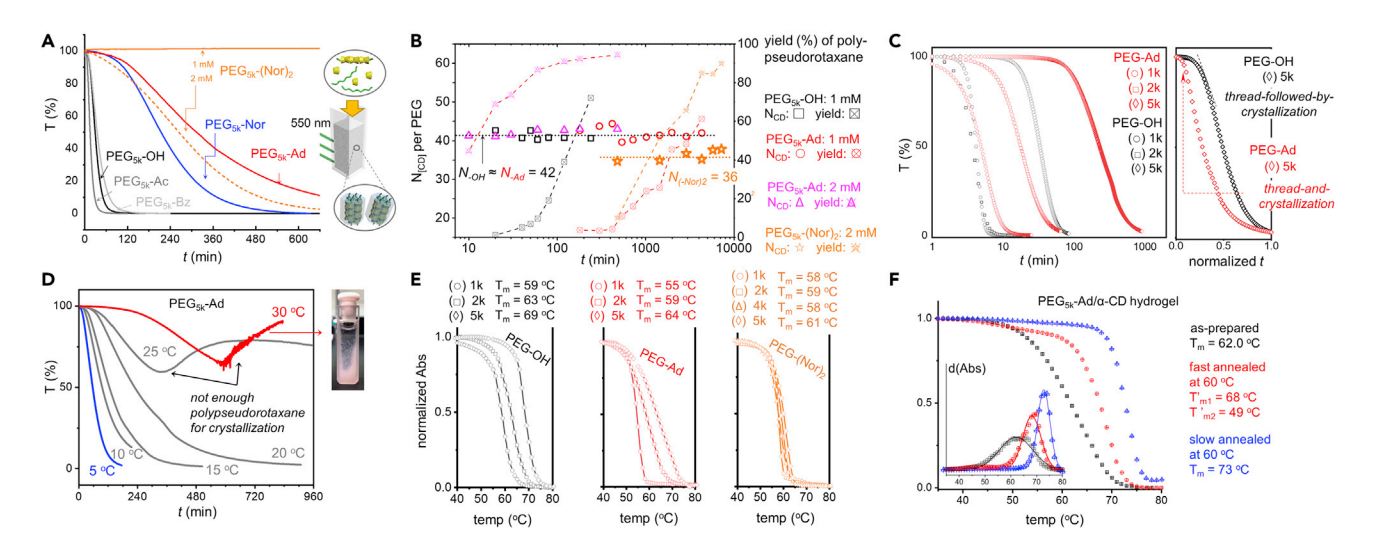


Figure 3. Kinetic investigations of the threading and translocation of  $\alpha$ -CDs on polymer axles and the crystallization of polypseudorotaxanes (A) Time-dependent transmittance of the reactions of  $\alpha$ -CD (50 mM, 100 mM for PEG<sub>5k</sub>-(Nor)<sub>2</sub>) and PEG<sub>5k</sub> (1 mM, 2 mM for PEG<sub>5k</sub>-(Nor)<sub>2</sub>) with different end groups at 20°C. I = 10 mm,  $\lambda = 550$  nm.

- (B)  $^{1}$ H NMR analysis of the threaded  $\alpha$ -CDs per PEG at different times and the measured yields of the polypseudorotaxanes.
- (C) Time-dependent transmittance and time-normalized transmittance (right) of the reactions of  $\alpha$ -CDs (50 mM) with PEG<sub>1-5k</sub>-OH, and PEG<sub>1-5k</sub>-Ad at 20°C, PEG<sub>1k</sub>, PEG<sub>2k</sub>, and PEG<sub>5k</sub> concentrations of 5, 2.5, and 1 mM, respectively, at 20°C.
- (D) Time-dependent transmittances of the reactions of  $\alpha$ -CD (50 mM) and PEG<sub>5k</sub>-Ad (1 mM) measured at different temperatures.
- (E) Temperature-dependent melting profiles and calculated  $T_m$  of polypseudorotaxane aggregates formed by  $\alpha$ -CD/PEG<sub>1-5k</sub>-OH,  $\alpha$ -CD/PEG<sub>1-5k</sub>-Ad, and  $\alpha$ -CD/PEG<sub>1-5k</sub>-(Nor)<sub>2</sub>. Heating rate: 1°C/min. I = 2 mm.
- (F) Melting profiles of a  $\alpha$ -CD/PEG<sub>5k</sub>-Ad polypseudorotaxane hydrogel in its as-prepared form (black), 60°C fast annealed (red) and slow annealed (blue) forms. I=1 mm. Samples were diluted by half to PEG<sub>5k</sub>-Ad (1 mM) and  $\alpha$ -CD (50 mM) for measurements. Inset: fitted  $T_m$ .

transmittance experiments (Figures 3D and S11) and their crystallization energy barrier  $^{30}$  difference was calculated as  $\Delta E'_{crys}$  -  $\Delta E_{crys}$  = -24 kJ/mol (Figures 1 and S12). The faster crystallization of PEG5k-Ad/ $\alpha$ -CD polypseudorotaxanes was evident in the early onset of transmittance decrease in the time-normalized transmittance spectra (Figure 3C), where the crystallization of PEG-Ad polypseudorotaxanes took place concurrently with the formation of the polypseudorotaxanes in solution, compared with the formation-followed-by-crystallization process in the case of the PEG-OH polypseudorotaxanes. Therefore, the raised energy barrier of PEG5k-Ad/ $\alpha$ -CD polypseudorotaxanes formation in solution and decreased energy barrier of crystallization enabled a concerted threading-and-crystallization process, where the as-formed polypseudorotaxanes were rapidly trapped by crystallization.

Despite PEG<sub>5k</sub>-OH/ $\alpha$ -CD and PEG<sub>5k</sub>-Ad/ $\alpha$ -CD polypseudorotaxanes having nearly identical numbers of threaded  $\alpha$ -CDs, the large differences of their assembly kinetics in solution and crystallization implied that PEG-Ad/ $\alpha$ -CD polypseudorotaxanes possess very different structures compared with the tubular PEG-OH/ $\alpha$ -CD polypseudorotaxanes. When the first few  $\alpha$ -CDs threaded on to PEG<sub>5k</sub>-Ad, the  $\alpha$ -CD/Ad side-on complexation drove these  $\alpha$ -CDs to translocate throughout the entire PEG axle to reach the -Ad end. This side-on complexation formation was confirmed as the binding affinity between an oligo-glycol adamantlyester 2EG-Ad and  $\alpha$ -CD was measured as  $K_a$  = 105 M<sup>-1</sup> at 25°C (Table S2; Figure S16), being larger than the affinity of  $K_a$  = 5 M<sup>-1</sup> for 2EG and  $\alpha$ -CD. Increasing the (EG)<sub>2</sub> moieties to 4EG-Ad and 6EG-Ad resulted in the binding affinities between  $\alpha$ -CD and every extended (EG)<sub>2</sub> moiety decreasing gradually (Table S2). When the PEG<sub>5k</sub>-Ad axle reached 5k Da, the later threaded  $\alpha$ -CDs could be segregated kinetically between coiled PEG segments at different locations (Figure 2) in which the coiled PEG axle





acted as a dynamic translocation energy barrier. To confirm this possibility, shorter PEG-OH and PEG-Ad axles (1k and 2k Da) were employed for the time-dependent polypseudorotaxanes formation experiments (Figure 3C). Reducing the axle length from 5k to 2k and 1 kDa, the formation and crystallization between PEG-Ad and PEG-OH polypseudorotaxanes became increasingly comparable, since less segmented  $\alpha$ -CD blocks could be kinetically trapped on shorter PEG-Ad axles.

When these polypseudorotaxanes with segmented  $\alpha$ -CD blocks crystallized before they reached the thermodynamically preferred tubular co-conformations in solution, these kinetically resolved polypseudorotaxanes were trapped as micro-crystallized meta-stable aggregates. This early crystallization could be attributed to faster diffusion and conformational relaxation<sup>32</sup> of the segmented  $\alpha$ -CD blocks. To assess the energy differences between the crystallized PEG<sub>5k</sub>-OH/α-CD and PEG<sub>5k</sub>-Ad/α-CD polypseudorotaxanes, melting curve analyses were carried out (Figures 3E and 3F). The melting points  $(T_m)$  were measured to reflect the energy required to extensively break the multivalent hydrogen bonding interactions of the crystalline domain (Table S3; Figures S23 and S24). Compared with a  $T_m = 69^{\circ}$ C and a narrow melting profile of PEG<sub>5k</sub>-OH/ $\alpha$ -CD, the lower  $T_m = 64$ °C and broader melting curve of PEG<sub>5k</sub>-Ad/α-CD (Figure 3E) suggest that less extensive hydrogen-bonding networks were formed in its crystalline domains. Annealing the PEG<sub>5k</sub>-Ad/ $\alpha$ -CD polypseudorotaxanes resulted in narrower melting profiles and higher  $T_m$  in PEG<sub>5k</sub>-Ad/ $\alpha$ -CD (Figure 3F). These experiments suggested that the formed PEG<sub>5k</sub>-Ad/α-CD polypseudorotaxanes are kinetic products with higher energies compared with their stable states. The broad melting profile of the as-prepared  $PEG_{5k}$ -Ad/ $\alpha$ -CD sample suggested that the PEG<sub>5k</sub>-Ad/ $\alpha$ -CD polypseudorotaxanes were constituted by a dispersed mixture of PEG $_{5k}$ -Ad/ $\alpha$ -CD co-conformers, which converged to the stable conformer during the annealing process. Furthermore, the melting temperature differences between the PEG-Ad/ $\alpha$ -CD and PEG-OH/ $\alpha$ -CD polypseudorotaxanes at shorter PEG axles were smaller (Figure 3E) since the translocation energy barriers for  $\alpha$ -CDs are decreased at short PEG axles.

When PEG-(Nor)<sub>2</sub> of different molecular weights were employed as axles, the bulky -Nor end groups reduced the rate of  $\alpha$ -CD (de)threading, resulting in fewer threaded  $\alpha$ -CDs per PEG<sub>5k</sub>-(Nor)<sub>2</sub> (a constant of 36  $\pm$  1  $\alpha$ -CDs, Figure 3B). Since the -Nor moieties also formed side-on complexes with  $\alpha$ -CDs (Table S2), less dispersed co-conformers of polypseudorotaxanes were trapped kinetically, featuring  $\alpha$ -CD blocks at each chain end and the middle of the PEG (Figure 2). This is evident in the narrow melting profiles of PEG<sub>1-Sk</sub>-(Nor)<sub>2</sub>/ $\alpha$ -CD polypseudorotaxanes (Figure 3E). Note that higher reactant concentrations are required to form crystalline polypseudorotaxane aggregates, which indicates that the crystallization threshold could be adjusted (i.e., reaction concentrations) to selectively trap polypseudorotaxanes in different kinetic states.

At higher concentrations,  $PEG_{5k}$ -Ad/ $\alpha$ -CD polypseudorotaxane ([ $PEG_{5k}$ -Ad] = 6 mM) formed much stronger hydrogels compared with  $PEG_{5k}$ -OH/ $\alpha$ -CD hydrogels<sup>33</sup> at various  $EG/\alpha$ -CD ratios (Figure 4A). When decreasing the  $EG/\alpha$ -CD ratio from 10:1 to 2:1 (more fed  $\alpha$ -CD, I to IV, Figure 4A), the elastic moduli of the hydrogels composed of  $PEG_{5k}$ -Ad/ $\alpha$ -CD increased first to a maximum G'=0.52 MPa at  $EG/\alpha$ -CD = 4:1 and then decreased. By changing the fed  $EG/\alpha$ -CD ratio from 10:1 to 4:1, the number of threaded  $\alpha$ -CDs increased from 15 to 28  $\alpha$ -CDs per PEG (Table S1). More segmented  $\alpha$ -CD blocks were kinetically trapped and crystallized, which increased the crosslinking density of the hydrogel networks to an optimized network density and crystalline domain size (III, Figure 4A). Further changing the  $EG/\alpha$ -CD





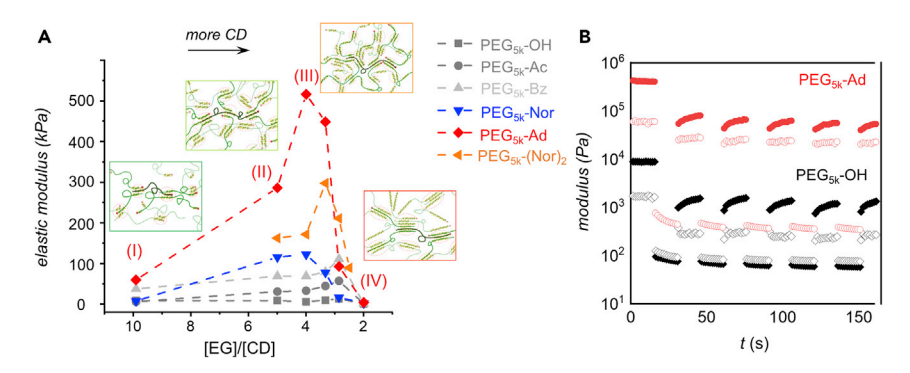


Figure 4. Rheological investigations of kinetically trapped polypseudorotaxane networks (A) Elastic moduli of polypseudorotaxane hydrogels measured by angular frequency sweeps. Hydrogels were prepared by mixing  $\alpha$ -CD (67 to 330 mM) and PEG<sub>5k</sub>-R (8 mM) at listed EG/ $\alpha$ -CD ratios.

(B) Step-strain rheological profiles of polypseudorotaxane hydrogels composed of PEG<sub>5k</sub>-OH/  $\alpha$ -CD and PEG<sub>5k</sub>-Ad/ $\alpha$ -CD at an EG/ $\alpha$ -CD ratio of 4:1. Alternating 0.1% and 100 % strain were applied to the sample every 15 s.

ratio to 2:1, the number of threaded  $\alpha$ -CDs increased to 44  $\alpha$ -CDs per PEG (Table S1), which significantly lowered the number of  $\alpha$ -CD blocks formed on the PEG axle and reduced the network crosslinking density (IV, Figure 4A). Similarly, a " $\Lambda$ "-shaped elastic moduli variation of hydrogels formed by PEG<sub>5k</sub>-(Nor)<sub>2</sub>/ $\alpha$ -CD were also measured at different EG/ $\alpha$ -CD ratios (Figure 4A). The maximum G′ = 0.30 MPa of PEG<sub>5k</sub>-(Nor)<sub>2</sub>/ $\alpha$ -CD hydrogel was recorded in EG/ $\alpha$ -CD = 3.3:1, in which an averaged 26  $\alpha$ -CDs were threaded on the axle (Table S1). In great contrast, the elastic moduli of PEG<sub>5k</sub>-OH/ $\alpha$ -CD polypseudorotaxane hydrogels demonstrated little change at various EG/ $\alpha$ -CD ratios, highlighting the differences of the polypseudorotaxane networks formed under kinetic (PEG<sub>5k</sub>-Ad/ $\alpha$ -CD and PEG<sub>5k</sub>-(Nor)<sub>2</sub>/ $\alpha$ -CD) and thermodynamic (PEG<sub>5k</sub>-OH/ $\alpha$ -CD) paths. Step-strain rheological experiments (Figures 4B and S27) showed that both PEG<sub>5k</sub>-Ad/ $\alpha$ -CD and PEG<sub>4-5k</sub>-Nor/ $\alpha$ -CD hydrogels exhibited rapid self-healing properties for 3D-printing, but PEG<sub>5k</sub>-OH/ $\alpha$ -CD hydrogels were not 3D-printable.

#### Structural analyses of α-CD/PEG polypseudorotaxanes

To structurally verify the segmented  $\alpha$ -CD blocks in the kinetically trapped polypseudorotaxanes hydrogels, small-, wide-angle X-ray diffractions (S/WAXS), and scanning electron microscopy (SEM) analyses were carried out. However, the widely adopted parallelly packed PEG/α-CD polypseudorotaxanes model<sup>34</sup> disfavors the crystallization of  $\alpha$ -CD blocks of different sizes (Figure S29). We, fortunately, obtained high-quality hexagonal single-crystals of PEG<sub>600</sub>-(OH)<sub>2</sub>/ $\alpha$ -CD polypseudorotaxanes (Figure 5A). For the first time, we revealed the molecular details of the crystalline domains. Two co-existing polymorphs of PEG $_{600}/\alpha$ -CD polypseudorotaxanes were consistently discovered as PEG<sub>600</sub>-(OH)<sub>2</sub>/ $\delta(\alpha$ -CD) and [(EG)<sub>4</sub>/ $2(\alpha$ -CD)]<sub>n</sub> complexes through a solvent evaporation method. The major polymorph PEG<sub>600</sub>- $(OH)_2/6(\alpha-CD)$  complex (Figure 5A) crystallized into a trigonal P3<sub>2</sub>21 space group with a = b = 23.7877 Å, c = 52.0858 Å. The minor polymorph [(EG)<sub>4</sub>/2( $\alpha$ -CD)]<sub>n</sub> complex (Figure 5A) crystallized into a P321 space group with a = b = 23.5446(15)Å, c = 15.7523 Å. In the PEG<sub>600</sub>-(OH)<sub>2</sub>/6( $\alpha$ -CD) complex, there are six  $\alpha$ -CDs hydrogen-bonded in a head-to-head and tail-to-tail manner on the PEG axle. The secondary faces of the two α-CDs located at the PEG chain end (blue colored, O●●●O = 6.45 and 6.71 Å, Figure 5A) are hydrogen-bonded via water molecules along the c-axis. In  $[(EG)_4/2(\alpha-CD)]_n$ , threaded  $\alpha$ -CDs on the PEG are tightly packed



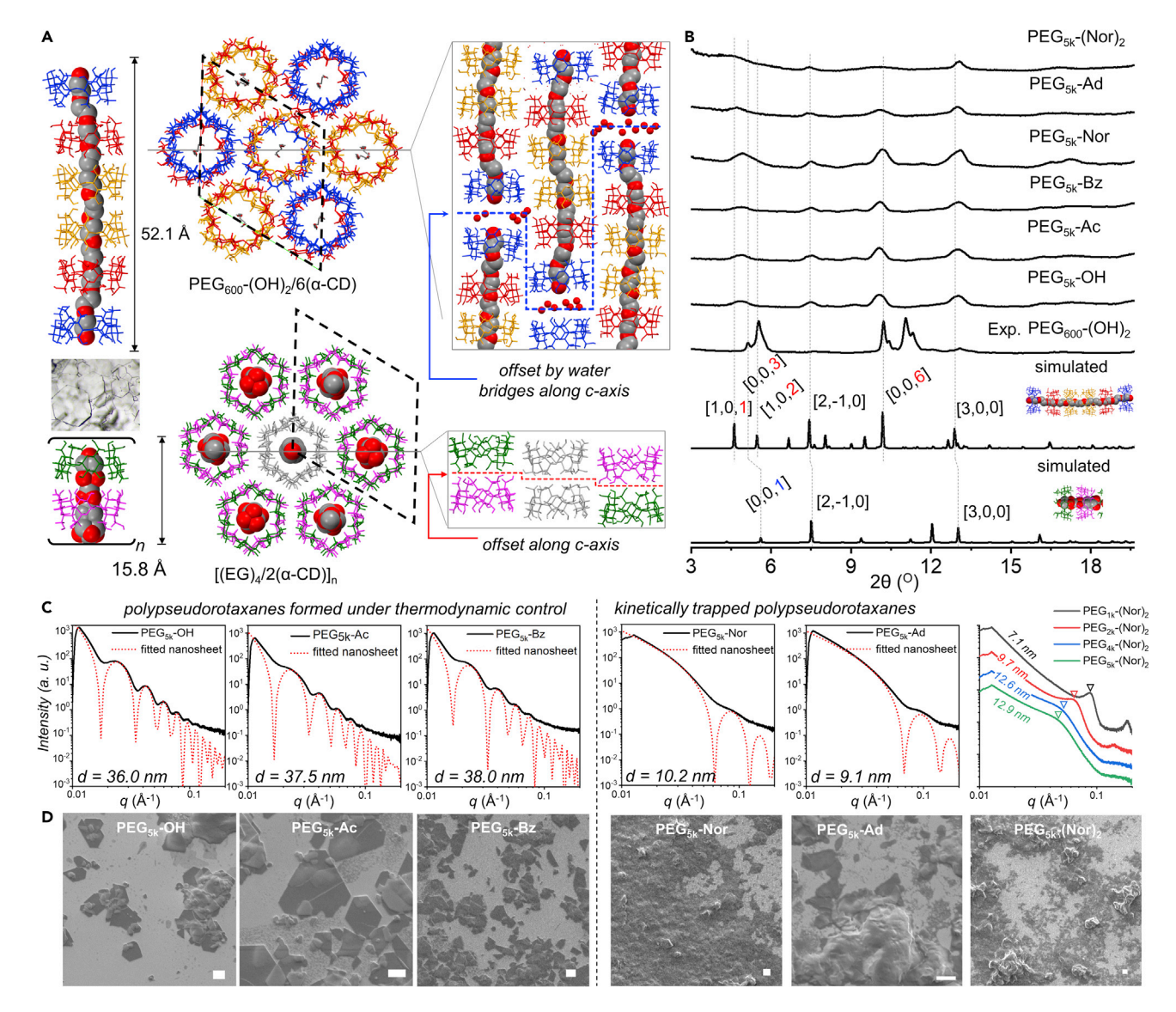


Figure 5. Structural and morphological analyses of  $\alpha\text{-CD/PEG}$  polypseudorotaxanes

- (A) Single-crystal structures of two polymorphs of polypseudorotaxane  $PEG_{600}$ -(OH) $_2/6(\alpha$ -CD) and  $[(EG)_4/2(\alpha$ -CD)] $_n$ .  $\alpha$ -CDs were color-coded to represent different symmetry equivalences.
- (B) WAXS profiles of the hydrogels formed by different  $\alpha$ -CD/PEG polypseudorotaxanes, the crystal sample of PEG<sub>600</sub>-(OH)<sub>2</sub>/ $\alpha$ -CD, and the simulated of PEG<sub>600</sub>-(OH)<sub>2</sub>/ $\delta(\alpha$ -CD) and [(EG)<sub>4</sub>/2( $\alpha$ -CD)]<sub>n</sub>.
- (C) SAXS profiles (solid line) of the hydrogels formed by different  $\alpha$ -CD/PEG polypseudorotaxanes (EG/ $\alpha$ -CD = 3.3:1) and their fitted curve (dotted line) and thickness. Polypseudorotaxanes are fitted to hexagonal sheet-like form factor, and  $\alpha$ -CD/PEG-(Nor)<sub>2</sub> polypseudorotaxanes are fitted to lamellar form factor.
- (D) SEM images of the hydrogels formed by different  $\alpha$ -CD/PEG polypseudorotaxanes; scale bar, 1  $\mu m$ .

continuously between two adjacent rings, and the  $PEG_{600}$  axles are crystallographically disordered along the c-axis. It is worth noting that the polypseudorotaxanes in both polymorphs were packed unparallel and offset along the c-axis (Figure 5A), which corrected the previously suggested parallel packing models without offsetting. The offset packing of polypseudorotaxanes could allow the co-crystallization of size ill-matched  $\alpha$ -CD blocks from different polypseudorotaxanes along the c-axis (Figure S29), similar to those double helices formed by ill-matched DNA base pairs. The offset packing of polypseudorotaxanes along the c-axis are crystallographically dispersion.





We used experimental and simulated WAXS profiles of PEG<sub>600</sub>-(OH)<sub>2</sub>/α-CD polypseudorotaxanes to index the diffraction profiles of the polypseudorotaxane hydrogels. In the PEG<sub>5k</sub>-OH/ $\alpha$ -CD, PEG<sub>5k</sub>-Ac/ $\alpha$ -CD, and PEG<sub>5k</sub>-Bz/ $\alpha$ -CD hydrogels (Figure 5B), similar diffraction peaks with their Miller indices were assigned as  $2\theta$  =  $5.0^{\circ}$  [0, 0, 3/],  $7.5^{\circ}$  [2, -1, 0],  $10.1^{\circ}$  [0, 0, 6/],  $13.0^{\circ}$  [3, 0, 0], in which / is an integral number reflecting different c-axis lengths. In PEG<sub>5k</sub>-Ad/α-CD hydrogel, the diffraction peaks at  $2\theta = 5^{\circ}$  and  $10.1^{\circ}$  were broadened, indicating that the c-axis of each crystalline domains in these hydrogels were dispersed. The structural differences of the crystalline domains formed in PEG<sub>5k</sub>-R/ $\alpha$ -CD with different end groups were more pronounced in small-angle X-ray (SAXS) and SEM analyses (Figures 5C and 5D). Clear fringes fitted to the sheet-like form factor of 36.0, 37.5, and 38.0 nm were recorded in PEG<sub>5k</sub>-OH/ $\alpha$ -CD, PEG<sub>5k</sub>-Ac/ $\alpha$ -CD, and PEG<sub>5k</sub>-Bz/ $\alpha$ -CD hydrogels, respectively, with sub-micron sized hexagonal sheet-like observed in SEM (Figure 5D). In contrast, fringes of kinetically trapped PEG<sub>5k</sub>-Ad/α-CD hydrogels were fitted to a sheet-like thickness of 9.1 nm with much fewer structural features, indicating that the segmented  $\alpha$ -CD blocks comprised about 10  $\alpha$ -CDs on average. In the PEG<sub>2k</sub>-Ad/α-CD hydrogel, diffraction fringes with better structural features were fitted to a sheet-like thickness of 15.8 nm (Figure S40), indicating that the crystalline domains formed using shorter PEG<sub>2k</sub>-Ad axle are larger and less disordered. SEM analysis showed the annealed sample of PEG<sub>5k</sub>-Ad/ $\alpha$ -CD polypseudorotaxane as micrometer-sized trigonal single-crystals (Figure S45), confirming the structural differences between the kinetic and thermodynamic outcomes. Similarly, the S/WAXS profiles of the PEG<sub>4/5k</sub>-(Nor)<sub>2</sub>/ $\alpha$ -CD hydrogels contained fewer structural details. Their structures were suggested as disordered lamellar assemblies by comparing to the clear fringes in shorter chain PEG<sub>1-2k</sub>-(Nor)<sub>2</sub>/α-CD hydrogels (Figures 5C and S41). When  $\alpha$ -CDs surmounted the -Nor speed bumps of shorter PEG<sub>1/2k</sub>-(Nor)<sub>2</sub>, they were concentrated locally at each chain end. When the PEG chain lengths were extended to PEG<sub>4/5k</sub>-(Nor)<sub>2</sub>, segmented  $\alpha$ -CD blocks at the chain ends and random sites of the chain emerged, which nucleated individually<sup>36</sup> to form branched meta-stable crystalline networks (Figure 2).

#### 3D-printing of polyrotaxane network hydrogels

The concerted kinetic trapping of polypseudorotaxane networks enabled the possibility to trap different network architectures from the same reactive ensemble. We chose to trigger an initial temperature difference to the PEG<sub>4k</sub>-(Nor)<sub>2</sub> and α-CD mixture at high concentrations to kinetically trap two meta-stable polypseudorotaxanes networks of different densities. They were subsequently covalently crosslinked as polyrotaxane networks. Experimentally, a hydrogel ink-1 (Figure 6A) composed of PEG<sub>4k</sub>-(Nor)<sub>2</sub> (22.5 mM),  $\alpha$ -CD (308 mM), tetrathiol crosslinker TTC (11.3 mM), and a photo-initiator was optimized with suitable viscoelasticity for 3D-printing (Figure S48). Ink-1 possesses a high elastic modulus of G' = 0.70MPa at 25°C (Figure 6B). By increasing the reaction temperature, the overall binding affinity between  $\alpha$ -CDs and PEG-(Nor) $_2$  decreased, which dismantled the original crystalline network, dethreaded some  $\alpha$ -CDs, and formed a new crystalline network. At 60°C for 1 h, the elastic modulus of ink-1 was reduced to 56 kPa but remained viscoelastic for 3D-printing. After rapid cooling to 25°C, the elastic modulus of ink-1 increased very slowly at ambient conditions (Figure 6B), suggesting that the meta-stable crystalline network formed at  $60^{\circ}$ C prevented rapid  $\alpha$ -CD rethreading at room temperature.

After thiol-ene crosslinking, the polypseudorotaxanes 3D-printed at  $20^{\circ}$ C and  $60^{\circ}$ C were converted to polyrotaxane network hydrogels (PNHs) as PNH-8 and PNH-3 (Figure 6C), respectively. An  $\alpha$ -CD-free hydrogel PNH-0 was also synthesized in



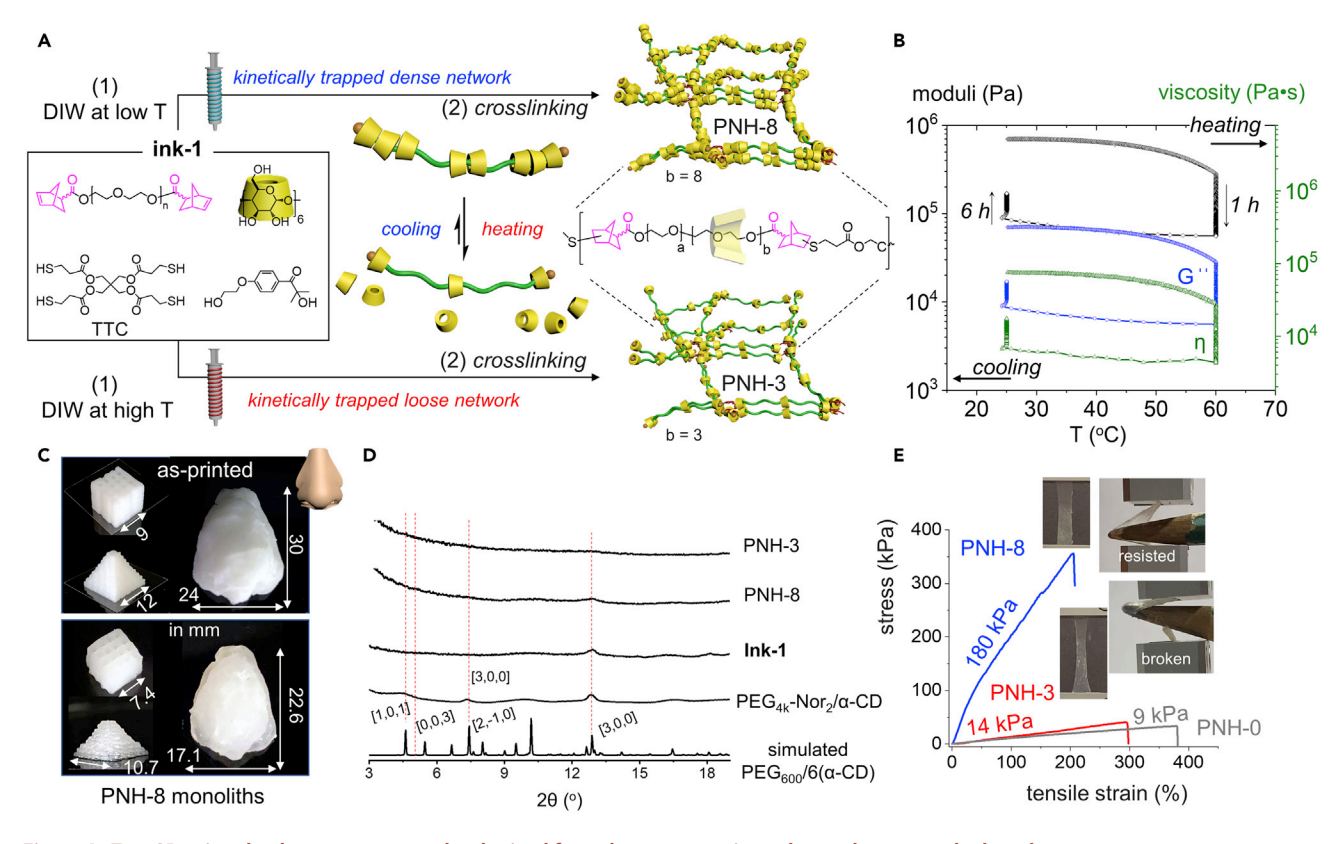


Figure 6. Two 3D-printed polyrotaxane networks obtained from the same reactive polypseudorotaxane hydrogel

- (A) Temperature-diverged formation of PNH-3 and PNH-8 after 3D-printing and photo-crosslinking.
- (B) Temperature-dependent elastic (black), loss moduli (blue), and viscosity (green) of ink-1, heating and cooling rates set as 3°C and 20°C/min.
- (C) As-printed hydrogels and their covalently crosslinked polyrotaxane monoliths.
- (D) WAXS profiles of hydrogels PEG<sub>4k</sub>-(Nor)<sub>2</sub>/ $\alpha$ -CD, ink-1, PNH-3, and PNH-8.
- (E) Tensile stress measurements of PNHs, rate: 0.1 mm/s. Inset: PNHs upon elongation and pencil penetration. PNH-0 was synthesized in a DMF solution in the absence of  $\alpha$ -CD.

DMF for reference (Figure S51). The averaged molar ratios of PEG<sub>4k</sub>-(Nor)<sub>2</sub>/ $\alpha$ -CD/TTC components in PNH-8 and PNH-3 were revealed by  $^1$ H NMR hydrolysis as 1:8.0  $\pm$  0.7:0.62  $\pm$  0.02 and 1:2.9  $\pm$  0.4:0.67  $\pm$  0.05, respectively (Table S13). The covalent network densities in these PNHs were similar, as suggested by the ratios of PEG<sub>4k</sub>-(Nor)<sub>2</sub>/TTC. There are eight  $\alpha$ -CDs per PEG in PNH-8, compared to only three  $\alpha$ -CDs per PEG in PNH-3. The WAXS profiles of PNHs were broad (Figure 6D), because fewer interlocked  $\alpha$ -CDs and the limited PEG chain diffusion in PNHs reduced their crystalline domain sizes proportionally, compared to the parent ink-1. At the macroscale, Young's moduli of PNH-0, PNH-3, and PNH-8 were measured as 9, 14, and 180 kPa, respectively (Figure 6E). PNH-3 showed slightly enhanced Young's moduli over PNH-0 due to its sparsely distributed hydrogenbonded crystalline network. PNH-8 was significantly tougher than PNH-3 in the pencil penetration test (Figure 6E; Videos S1 and S2) benefiting from its denser crystalline network formed by more interlocked  $\alpha$ -CDs.

The different numbers of interlocked  $\alpha$ -CDs in PNH hydrogels gave them different moisture-responsiveness at varied relative humidities (RH). When PNH-3 and PNH-8 were placed in sealed chambers of different RH, PNH-3 swelled to 270% at RH = 58% with significantly reduced Young's moduli (Figure 7A). In comparison, PNH-8 showed better resistance to humidity change, since its denser crystalline network





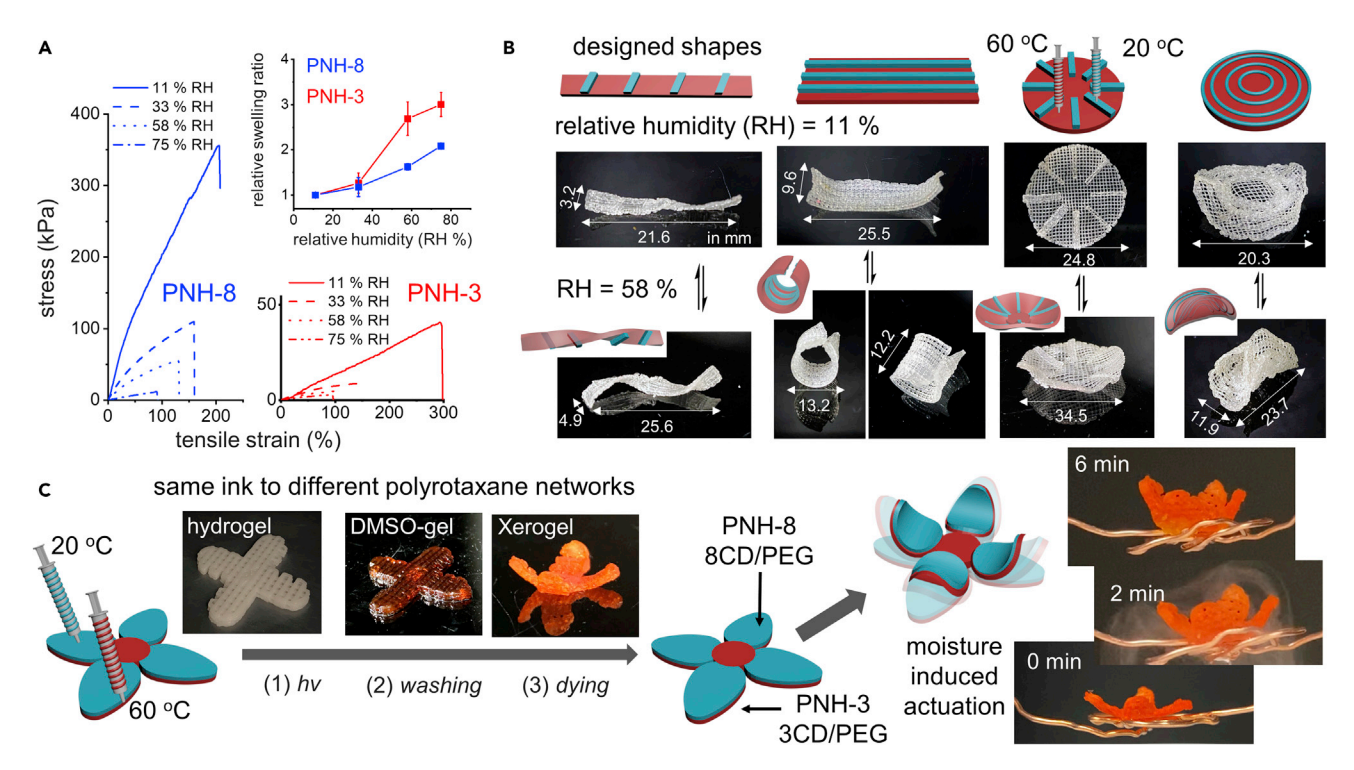


Figure 7. 3D-printed heterogeneous polyrotaxane actuators and their moisture-responsive shape-morphing behaviors

(A) Tensile stress measurements of PNH hydrogels equilibrated at different relative humidity (11%, 33%, 58%, and 75%), respectively, rate: 0.1 mm/s. Inset: relative swelling ratios of PNHs at different relative humidity. The error bars were derived from three individual experiments.

(B) Designed dual-material actuator models (top), the fabricated (3D-printing followed by crosslinking and washing) heterogeneous hydrogels at relative humidity 11% (middle), and their morphed shapes in the chamber of relative humidity = 58% (bottom). These heterogeneous hydrogels were fabricated using identical ink-1 printed at 20°C (green) and 60°C (red), respectively.

(C) 3D fabrication of a flower model using ink-1 printed at 20°C (green) and 60°C (red) followed by crosslinking. The afforded polyrotaxane flower demonstrated folding motions upon moistening due to the spatial integration of PNH-3 and PNH-8 at the top and bottom layers.

formed by segmented  $\alpha$ -CD blocks competed against the osmatic pressure variation upon moisturizing.

By designing the 3D-printing script, <sup>37</sup> a series of heterogeneous lattices (Figure 7B) were 3D printed using the 60°C ink-1 (green) and the 20°C ink-1 (red), followed by photo-crosslinking. At a low RH of 11%, the lattices resembled their as-printed shapes (Figure 7B, middle). After being placed in a closed chamber at RH = 58%, they morphed into different shapes as designed (Figures 7B and S60-S64). When ink-1 was 3D-printed into a flower model (Figure 7C; Video S3), its lower section and the core were printed using the 60°C ink-1 and the top section was printed using the 20°C ink-1. After photo-crosslinking, the compositions of the heterogeneous polyrotaxane flower was revealed as PEG<sub>4k</sub>-(Nor)<sub>2</sub>: $\alpha$ -CD ratios of 1:7.6  $\pm$  0.5 and 1:3.5  $\pm$  0.2 for the top and bottom sections, respectively. The dried flower (Figure 7C) bent slightly inwards due to the higher density of the  $\alpha$ -CD crystalline domains in the top section. When this monolith was exposed to moisture, it folded inward in 6 min (Figure 7C; Video S4). During this process, the top layer possessing a denser  $\alpha$ -CD crystalline network persisted against osmatic pressure variation, but the bottom layer swelled quickly due to the solvation of its mostly unthreaded PEG and sparse crystalline network. Shape-morphing in response to the relative humidity change enabled the fabrication of environmentally controlled actuators with low energy consumption, <sup>38</sup> providing a sustainable solution for the development of smart devices. 39,40





#### **DISCUSSION**

In summary, our discovery demonstrated a chemical approach to synthesize 3Dprintable poly(pseudo)rotaxane materials through a concerted kinetic coupling of polypseudorotaxane formation in the solution phase with their micro-crystallization in the gel phase. Through the installation of sterically demanding end groups on PEG, we created kinetic barriers for  $\alpha$ -CDs threading and translocation, and resolved a spectrum of previously transient states in the solution phase. These polypseudorotaxanes with segmented  $\alpha$ -CD blocks possess lower kinetic barriers for micro-crystallization, forming polypseudorotaxane hydrogels with different network architectures. We demonstrated that the kinetically trapped PEG-Ad/α-CD and PEG-Nor<sub>2</sub>/ $\alpha$ -CD polypseudorotaxanes form less-ordered  $\alpha$ -CD blocks on the PEG axles. Our single-crystal X-ray analysis of PEG-OH<sub>2</sub>/α-CD polypseudorotaxanes corrected the long-standing misunderstanding of the packing models of polypseudorotaxanes. The revealed unparallel packing of polypseudorotaxanes indicated the possibility of forming crystalline domains using length varied  $\alpha$ -CD blocks in our kinetic synthesis. Furthermore, we demonstrated a simultaneous variation of polypseudorotaxane network architecture using the same reactive ensemble at different temperatures. After dual-material 3D printing followed by chemical crosslinking, 3D-printed heterogeneous lattices demonstrated moisture responsive actuations, which was enabled by the two polyrotaxane materials possessing different numbers of  $\alpha$ -CDs at the nanoscale, different crystalline domains at the mesoscale, and different mechanical properties at the macroscale. Our work not only showcased a concerted kinetic trapping approach capable of synthesizing materials in their higher energy states but also demonstrated a path to use less-ordered molecular assemblies that were previously considered disadvantageous to construct supramolecular polymer materials with superior properties. In addition, we successfully synthesized kinetically stable hydrogels using medium to low molecular weight PEG derivatives ( $\leq$ 5 kDa), which overcame a long-standing obstacle in biomedical applications because current stable hydrogels formed by large molecular weight PEG presented problems<sup>41</sup> to be filtered out by human kidneys.<sup>42</sup>

#### **EXPERIMENTAL PROCEDURES**

#### Resource availability

#### Lead contact

Further information and requests for resources should be directed to and will be fulfilled by the lead contact, Chenfeng Ke (chenfeng.ke@dartmouth.edu).

#### Materials availability

All unique reagents generated in this study are available from the lead contact without restriction.

#### Data and code availability

The X-ray datasets generated during this study are available at the Cambridge Crystallographic Data Centre (CCDC) <a href="https://www.ccdc.cam.ac.uk">https://www.ccdc.cam.ac.uk</a> under deposition numbers 2008413 and 2008415. The 3D printing scripts generated in this study are available from the lead contact.

#### Time-dependent <sup>1</sup>H nuclear magnetic resonance experiments

To understand the crystallization process and examine the components remaining in the solution phase, time-dependent  $^1H$  NMR experiments were performed on reactions of polypseudorotaxane formed by  $\alpha$ -CD (50 mM)/PEG<sub>5k</sub>-OH (1 mM) or  $\alpha$ -CD (50 mM)/PEG<sub>5k</sub>-Ad (1mM) in D<sub>2</sub>O. D<sub>2</sub>O solutions of PEG<sub>5k</sub>-OH (2 mM) or PEG<sub>5k</sub>-Ad (2 mM) were added to NMR tubes to acquire their proton resonances. Upon





the addition of  $\alpha$ -CD (50 mM), periodic acquisitions (every 10 min for PEG<sub>5k</sub>-OH and 30 min for PEG<sub>5k</sub>-Ad) were performed until correspondent polypseudorotaxane formed a hydrogel-like aggregate and broadened the <sup>1</sup>H NMR signal (160 min for PEG<sub>5k</sub>-OH and 15 h for PEG<sub>5k</sub>-Ad).

#### Binding affinities and stoichiometries measurements

The binding affinities and stoichiometries of the complexes formed between Nor- $CO_2Na$ , 2EG-Ad, 4EG-Ad, 6EG-Ad, and  $\alpha$ -CD were measured by <sup>1</sup>H NMR titration. D<sub>2</sub>O solutions of Nor-CO<sub>2</sub>Na or nEG-Ad (n = 2, 4, 6, 2.0 mM) were titrated with  $\alpha$ -CD solutions. The  $\alpha$ -CD solutions (20, 40 and 60 mM respectively for n = 2, 4, 6) were prepared by dissolving  $\alpha$ -CD in a Nor-CO<sub>2</sub>Na or nEG-Ad (2.0 mM) D<sub>2</sub>O solution. The binding constant between Nor-CO<sub>2</sub>Na and α-CD was fitted using the algorithms provided by Supramolecular.org 43 using a 1:1 binding model. Binding constants between 2/4EG-Ad and  $\alpha$ -CD were fitted using the algorithms in a 1:1 binding model and 1:2 binding model (full and additive). The 1:3 binding model for  $\delta$ EG-Ad and  $\alpha$ -CD was accessed using MATLAB provided by literature with a minor adaptation to NMR titration. Job's plots were performed on the complexes formed between 4EG-Ad, 6EG-Ad and α-CD, revealing the formation of 1:2 and 1:3 complexes, respectively. To elucidate the binding affinities between nEG-Ad (n = 2, 4, 6) and  $\alpha$ -CD, and to simplify the binding models as a result of the calculation complexity, we employed several binding models to fit the binding between nEG-Ad (n = 2, 4, 6) and  $\alpha$ -CD, including a full binding model, additive binding model, non-cooperative binding model, and statistical binding model.

#### Transmittance monitoring of the formation of polypseudorotaxanes

Transmittance monitoring of the formation of polypseudorotaxanes was performed on a Shimadzu UV-vis spectrophotometer (UV-1800) with a Thermal CUBE solidstate cooling system for thermal control between 5.0°C and 90.0°C with temperature precision of 0.1°C, and optical lengths for general turbidity measurements and hydrogel melting experiments were set as 10 and 2 mm, respectively. When  $\alpha$ -CDs are threaded onto the PEG axles, less-soluble polypseudorotaxanes are formed and they crystallize as crystalline precipitates. The reaction turned from transparent to opaque. To understand the cascade threading and crystallization kinetic processes, a time-dependent reaction transmission change was monitored by UV-vis light scattering upon the mixing solutions of  $\alpha$ -CD and PEG-R from 100% transmittance to less than 1%. In typical time-dependent transmittance monitoring experiments, the reaction cuvette (optical length: 10 mm) was added with PEG<sub>5k</sub>-R (1, 2 mM for one case of PEG-(Nor)2, after mixing) with various end groups and α-CD (50, 100 mM for one case of PEG-(Nor)<sub>2</sub>, after mixing) at 20°C. The transmittance was monitored at 550 nm, accounting for the size of polypseudorotaxanes for appropriate Rayleigh scattering.<sup>29</sup> The data were acquired every 30 s until the transmittance was less than 1%.

#### Temperature-dependent absorbance profiles

The temperature-dependent absorbance profiles (melting curve) of polypseudoro-taxanes hydrogels formed by PEG<sub>1-5k</sub>-R with various end groups and different molecular weights (PEG-OH or PEG-Ad: 5, 2.5, 1 mM for 1, 2, 5 kDa respectively; PEG-(Nor)<sub>2</sub>: 5, 2.5, 1.25, 1 mM for 1, 2, 4, 5 kDa respectively, after mixing) and  $\alpha$ -CD (50 mM, 100 mM for PEG-(Nor)<sub>2</sub>, after mixing) was analyzed as follows: (1) the absorbance was normalized by defining the largest absorbance as 1.0 and the smallest absorbance as 0. (2) The first derivative of the absorbance profile was calculated quantitatively. (3) The derivatized data points were fitted by a Gaussian





function to generate the fitting parameters as the expected phase transition temperature  $T_m$  (melting point) and phase transition temperature variance  $\sigma_T$ .

#### Annealing of polypseudorotaxanes

The kinetically formed polypseudorotaxanes were annealed at different conditions and the corresponding melting experiments were performed. PEG<sub>5k</sub> with various end groups (PEG<sub>5k</sub>-R: 2 or 4 mM, after mixing) and  $\alpha$ -CD (100 or 113.6 mM, after mixing) were mixed in reaction vials to form the corresponding polypseudorotaxane hydrogels (EG/CD = 2.2:1 or 4:1) at 20°C and stabilized overnight. The as-prepared samples were heated at 60°C for 1 h and naturally cooled down in the air, or cooled down slowly in a temperature-controlled programmable oven over a period of 16 or 40 h (cooling ramp: 60°C–50°C:1°C/h, 50°C–20°C: 3°C/h or 60°C–20°C: 1 °C/h). Samples were diluted by half to PEG (1 or 2 mM) and  $\alpha$ -CD (50 or 56.8 mM) for each measurement. We employed higher concentrations of reactants to form kinetically generated products for annealing followed by dilution because the higher concentration formed products could not be dissolved at the annealing temperatures.

#### Rheological measurements

Rheological measurements were performed on a stress-controlled rheometer (TA instruments, DHR-2) with a 20-mm diameter parallel plate geometry and a measuring gap of 1 mm at 20°C. All polypseudorotaxane hydrogel samples were consolidated for at least 12 h at 20°C before the analysis unless otherwise specified. Strain sweep tests were performed to investigate the linear viscoelastic regions of the obtained polypseudorotaxane hydrogels at 25°C. The oscillation strain was increased from 0.01% to 100%. The angular frequency was set at 1 rad/s (frequency = 0.16 Hz). Angular frequency sweep tests were performed to investigate the elastic (storage) and viscous (loss) moduli at 25°C. The angular frequency was increased from 0.1 to 100 rad/s (frequency increased from 0.016 to 15.92 Hz). Based on the results of oscillation strain sweep experiments, the oscillation strain was set at 0.1%. Dynamic step-strain amplitude tests were performed to investigate the self-healing properties of the polypseudorotaxane hydrogels. The oscillation strain applied was 1% and 100% in each cycle at 1 rad/s angular frequency. The duration of strain at each step was 15 s. Steady rate sweep tests were carried out to investigate the shear-thinning behaviors of the polypseudorotaxane hydrogels at 25°C. The shear rate was increased from 1 to 100 s<sup>-1</sup>. The elastic, loss moduli, and viscosity of ink-1 were measured at a frequency of 1  $rad \cdot s^{-1}$  and a strain of 0.05% between 25°C and 60°C. The temperature-ramp contained a slow heating step from 25°C to  $60^{\circ}$ C at  $3^{\circ}$ C/min with an equilibrium time of 60 s for each temperature measurement, an isotherm step at 60°C for 1 h, a fast cooling step from 60°C to 25°C at 20°C/min, and an isotherm at 25°C for 6 h. To test the self-healing properties of ink-1 at 25°C and 60°C, step-strain tests were performed with alternating 0.1% and 100% strain applied to the samples every 15 s.

#### Single crystal analysis

Single crystals of PEG $_{600}/\alpha$ -CD polypseudorotaxanes suitable for single-crystal X-ray analysis were obtained by slow evaporation of an aqueous solution of a mixture of PEG $_{600}$ -(OH) $_2$  and  $\alpha$ -CD in 1:3 molar ratio (EG/CD = 4.21) over 7 days. Two polymorphs were identified in the same crystallization vial. Data were collected at 20°C in a Rigaku four circle supernova charge-coupled device (CCD) diffractometer with CuKa ( $\lambda$  = 1.54184 Å) radiation or Rigaku Xtalab mini II with MoKa ( $\lambda$  = 0.71073 Å) radiation, working at 50 kV and 12 mA. Data were collected and processed using CrysAlis Pro software.





#### Wide-angle X-ray analysis (WAXS) and small-angle X-ray analysis (SAXS)

WAXS and SAXS experiments were carried out using a Rigaku NANOPIX instrument with a Hypix-3000 detector. The water dispersions (or hydrogels) of the polypseudorotaxanes were poured into a glass capillary for X-ray measurements (WJM-glass/Muller borosilicate capillary:  $\phi = 2.0 \times \text{length} = 80 \text{ mm}$ ) and used for SAXS and WAXS measurements. The sample-to-detector distance was calibrated with a silver behenate diffraction peak. The sheet-like form factors were fitted to the experimental SAXS profiles in the manuscript using the Igor Macros. 44

#### Scanning electron microscope (SEM) imaging

SEM observation was conducted with a JEOL JSM-7800F microscope. The samples for SEM analyses were prepared by dipping a silicon oxide substrate into the water dispersion (or hydrogel) of the polypseudorotaxanes samples.

#### **Tensile tests**

Tensile tests were performed on a DHR2 system (TA instruments®, New Castle, DE) with a 50 N load cell following the ATSM D638. Ink-1 was preheated at 60 °C for 1 h and injected into a Teflon mold with a rectangular shape (40 x 8 x 2 mm). The molded samples were photo-crosslinked by UV irradiation ( $\lambda$  = 365 nm) at 20°C for 30 min, followed by a washing process with an excess of DMSO. Freshwater was introduced to exchange DMSO for 3 times. After washing, the samples were placed in a sealed container with a saturated LiCl solution (relative humidity 11%) at 20°C for 48 h. The 20°C sample was prepared similarly without pre-heating. A tensile axial load was applied to the molded sample at a rate of 0.1 mm/s until failure occurred. The Young's moduli of the specimens were calculated by fitting the linear equation of the stress-strain curve before the samples yielded. The elongation process was recorded by a digital camera. Pencil penetration tests were performed using PNH-3 and PNH-8 specimens prepared in the tensile tests. The specimens were fixed by two clamps. A pencil was used to apply pressure to the fixed samples. The process was recorded by a digital camera. Optical images were recorded by a consumer-grade camera.

#### Preparation of ink-1

PEG<sub>4k</sub>-(Nor)<sub>2</sub> (90 mg/mL, 22.5 mM),  $\alpha$ -CD (300 mg/mL, 308 mM), tetrathiol crosslinker TTC (5.5 mg/mL, 11.3 mM), and photo-initiator Irgacure D-2959 (33.3 mg/mL, 148 mM) were dissolved in H<sub>2</sub>O. The reaction mixture was stirred at 60°C for 30 min, then transferred to a syringe. The ink was cooled naturally to 20°C and was further consolidated for 48 h before being loaded to the 3D-printer. To analyze the number of threaded  $\alpha$ -CDs in ink-1, the hydrogel was quickly diluted by 3-fold with water and the mixture was centrifuged at 7,000 rpm for 2 min. The dilution and centrifugation processes were repeated two additional times. The collected white precipitate was lyophilized for <sup>1</sup>H NMR analysis and the ratio of  $\alpha$ -CD to PEG<sub>4k</sub>-(Nor)<sub>2</sub> was calculated as 12.9:1 (EG/ $\alpha$ -CD = 7.1:1), compared to the feeding ratio of  $\alpha$ -CD:PEG = 13.7 (EG/ $\alpha$ -CD = 6.6:1).

#### 3D printing

Ink-1 was loaded into syringes equipped to the BioAssemblybot 3D-printer. The printing scripts were generated by CAD software and Advanced Solution. The printing speed varied between 5–40 mm/s. High-temperature 3D-printing was conducted using BioAssemblybot 3D-printer equipped with a heating nozzle. Before printing, the heating nozzle was preheated at 60°C for 1 h. The printed monoliths were photo-crosslinked by UV irradiation ( $\lambda$  = 365 nm) at 20°C for 0.5–1 h, depending on the size of the printed objects. After photo-crosslinking, the monoliths were





immersed in an excess of DMSO until they became transparent. Subsequently, DMSO was decanted and water was added to exchange the solvent. The water bath was refreshed three times. The hydrogel was then immersed in an acetone bath for 2 h and transferred to a heated chamber to remove the acetone quickly, affording the xerogel. To analyze the compositions of polyrotaxane network, dried hydrogel samples prepared at 20°C and 60°C were hydrolyzed in 5% (v/v) NaOD/  $D_2O$  until no insoluble residuals were found in the NMR tube. Three samples at each temperature were prepared for  $^1H$  NMR hydrolysis measurements. PEG\_4k: tetra-SH:  $\alpha$ -CD ratios of PNH-8 and PNH-3 were measured as 1:0.62  $\pm$  0.02:8.0  $\pm$  0.7 and 1:0.67  $\pm$  0.05:2.9  $\pm$  0.4, respectively.

#### Flower model design and 3D-fabrication

A printer equipped with a 60°C and a 20°C nozzle was filled with ink-1. A flower model with a bilayer structure was designed. Its lower section and the core were printed using the heated ink, and its top section was printed using the 20°C ink. The flower model was photo-crosslinked by UV-irradiation ( $\lambda$  = 365 nm) for 1 h. After photo-crosslinking, the monoliths were immersed in an excess of DMSO until the objects became completely transparent. The DMSO was decanted and a rhodamine b (0.2 mM) DMSO solution was added to dye the DMSO-gel for imagining. The DMSO-gel was transferred to an aqueous bath (washed 3 times) and redyed using a rhodamine B (0.2 mM) aqueous solution. The hydrogel was then immersed in a rhodamine B (0.2 mM) acetone bath for 2 h and then placed in a heated chamber to evaporate the acetone quickly. To analyze the average number of threaded  $\alpha$ -CDs per PEG in the flower model, the samples were hydrolyzed in 5% (v/v) NaOD/D<sub>2</sub>O until no insoluble residuals were found in the NMR tube. Three additional samples of each section were prepared and hand-cut for  $^1$ H NMR hydrolysis.

#### Moisture induced actuation

The dyed xerogel was placed on a copper wireframe. A humidifier was placed 5 cm underneath the frame. Moisture was introduced and the process was recorded by a digital camera.

#### SUPPLEMENTAL INFORMATION

Supplemental information can be found online at https://doi.org/10.1016/j.chempr. 2021.06.004.

#### **ACKNOWLEDGMENTS**

C.K., M.T., and L.L. thank the Beckman Young Investigator Program. Q.L. and L.L. were partly supported by NSF EPSCoR-1757371. J.S. was supported by the NSF DMR-1844920. S.U. and K.I. were supported by JST-Mirai Program grant number JPMJMI18A2; JSPS KAKENHI grant numbers JP19H00907, JP21K14477, and JP19J12840; and OPERANDO-OIL. We thank Dr. Rina Maeda (formerly at the University of Tokyo) for the helpful discussion.

#### **AUTHOR CONTRIBUTIONS**

C.K. conceived the idea and wrote the manuscript. K.I. and S.U. assisted in editing. L.L. and M.T. initiated and conducted the polymer synthesis and kinetic studies with assistance from L.Z. Q.L. conducted the 3D printing and materials investigations. S.U. conducted the X-ray and SEM studies. J.S., C.K., S.L., and X.J. conducted the single-crystal studies.





#### **DECLARATION OF INTERESTS**

The authors have filed a provisional patent application US 63/021,971 on the 3D-printable polyrotaxanes.

Received: November 11, 2020 Revised: January 12, 2021 Accepted: June 3, 2021 Published: June 29, 2021

#### **REFERENCES**

- Fujita, D., Ueda, Y., Sato, S., Mizuno, N., Kumasaka, T., and Fujita, M. (2016). Selfassembly of tetravalent Goldberg polyhedra from 144 small components. Nature 540, 563–566. https://doi.org/10.1038/nature20771.
- Zhang, Z., Li, Y., Song, B., Zhang, Y., Jiang, X., Wang, M., Tumbleson, R., Liu, C., Wang, P., Hao, X.-Q., et al. (2020). Intra- and intermolecular self-assembly of a 20-nm-wide supramolecular hexagonal grid. Nat. Chem. 12, 468–474. https://doi.org/10.1038/s41557-020-0454-7
- Yan, X., Wang, F., Zheng, B., and Huang, F. (2012). Stimuli-responsive supramolecular polymeric materials. Chem. Soc. Rev. 41, 6042– 6065. https://doi.org/10.1039/C2CS35091B.
- Feng, L., Jia, S.S., Chen, Y., and Liu, Y. (2020). Highly elastic slide-ring hydrogel with good recovery as stretchable supercapacitor. Chemistry 26, 14080–14084. https://doi.org/10. 1002/chem.202001729.
- Li, Z., Pradeep, K.G., Deng, Y., Raabe, D., and Tasan, C.C. (2016). Metastable high-entropy dual-phase alloys overcome the strengthductility trade-off. Nature 534, 227–230. https://doi.org/10.1038/nature17981.
- Nagabhushana, G.P., Shivaramaiah, R., and Navrotsky, A. (2016). Direct calorimetric verification of thermodynamic instability of lead halide hybrid perovskites. Proc. Natl. Acad. Sci. USA 113, 7717–7721. https://doi. org/10.1073/pnas.1607850113.
- Pulido, A., Chen, L., Kaczorowski, T., Holden, D., Little, M.A., Chong, S.Y., Slater, B.J., Mcmahon, D.P., Bonillo, B., Stackhouse, C.J., et al. (2017). Functional materials discovery using energy-structure-function maps. Nature 543, 657–664. https://doi.org/10.1038/ nature21419.
- van Rossum, S.A.P., Tena-Solsona, M., van Esch, J.H., Eelkema, R., and Boekhoven, J. (2017). Dissipative out-of-equilibrium assembly of man-made supramolecular materials. Chem. Soc. Rev. 46, 5519–5535. https://doi.org/10. 1039/C7CS00246G.
- 9. Foy, J.T., Li, Q., Goujon, A., Colard-Itté, J.R., Fuks, G., Moulin, E., Schiffmann, O., Dattler, D., Funeriu, D.P., and Giuseppone, N. (2017). Dual-light control of nanomachines that integrate motor and modulator subunits. Nat. Nanotechnol. 12, 540–545. https://doi.org/10. 1038/nnano.2017.28.
- Gu, Y., Alt, E.A., Wang, H., Li, X., Willard, A.P., and Johnson, J.A. (2018). Photoswitching topology in polymer networks with metal-

- organic cages as crosslinks. Nature *560*, 65–69. https://doi.org/10.1038/s41586-018-0339-0.
- Li, Q., Fuks, G., Moulin, E., Maaloum, M., Rawiso, M., Kulic, I., Foy, J.T., and Giuseppone, N. (2015). Macroscopic contraction of a gel induced by the integrated motion of lightdriven molecular motors. Nat. Nanotechnol. 10, 161–165. https://doi.org/10.1038/nnano. 2014.315.
- Chen, J., Leung, F.K.-C., Stuart, M.C.A., Kajitani, T., Fukushima, T., van der Giessen, E., and Feringa, B.L. (2018). Artificial muscle-like function from hierarchical supramolecular assembly of photoresponsive molecular motors. Nat. Chem. 10, 132–138. https://doi. org/10.1038/nchem.2887.
- Odahara, J., Sun, W., Miura, A., Rosero-Navarro, N.C., Nagao, M., Tanaka, I., Ceder, G., and Tadanaga, K. (2019). Self-combustion synthesis of novel metastable ternary molybdenum nitrides. ACS Materials Lett 1, 64–70. https://doi.org/10.1021/ acsmaterialslett.9b00057.
- Aykol, M., Dwaraknath, S.S., Sun, W., and Persson, K.A. (2018). Thermodynamic limit for synthesis of metastable inorganic materials. Sci. Adv. 4, eaaq0148. https://doi.org/10.1126/ sciadv.aaq0148.
- Wehner, M., and Würthner, F. (2020). Supramolecular polymerization through kinetic pathway control and living chain growth. Nat. Rev. Chem. 4, 38–53. https://doi.org/10.1038/ s41570-019-0153-8.
- Sorrenti, A., Leira-Iglesias, J., Markvoort, A.J., de Greef, T.F.A., and Hermans, T.M. (2017). Non-equilibrium supramolecular polymerization. Chem. Soc. Rev. 46, 5476– 5490. https://doi.org/10.1039/C7CS00121E.
- Tantakitti, F., Boekhoven, J., Wang, X., Kazantsev, R.V., Yu, T., Li, J., Zhuang, E., Zandi, R., Ortony, J.H., Newcomb, C.J., et al. (2016). Energy landscapes and functions of supramolecular systems. Nat. Mater. 15, 469–476. https://doi.org/10.1038/nmat4538.
- Cheng, C., McGonigal, P.R., Schneebeli, S.T., Li, H., Vermeulen, N.A., Ke, C., and Stoddart, J.F. (2015). An artificial molecular pump. Nat. Nanotechnol. 10, 547–553. https://doi.org/10. 1038/nnano.2015.96.
- Groppi, J., Casimiro, L., Canton, M., Corra, S., Jafari-Nasab, M., Tabacchi, G., Cavallo, L., Baroncini, M., Silvi, S., Fois, E., and Credi, A. (2020). Precision molecular threading/ dethreading. Angew. Chem. Int. Ed. Engl. 59,

- 14825–14834. https://doi.org/10.1002/anie. 202003064.
- Qiu, Y., Song, B., Pezzato, C., Shen, D., Liu, W., Zhang, L., Feng, Y., Guo, Q.H., Cai, K., Li, W., et al. (2020). A precise polyrotaxane synthesizer. Science 368, 1247–1253. https:// doi.org/10.1126/science.abb3962.
- Truby, R.L., and Lewis, J.A. (2016). Printing soft matter in three dimensions. Nature 540, 371–378. https://doi.org/10.1038/nature21003.
- Harada, A., Li, J., and Kamachi, M. (1993). Preparation and properties of inclusion complexes of polyethylene glycol with.alpha.cyclodextrin. Macromolecules 26, 5698–5703. https://doi.org/10.1021/ma00073a026.
- Harada, A., Li, J., and Kamachi, M. (1993).
  Synthesis of a tubular polymer from threaded cyclodextrins. Nature 364, 516–518. https://doi. org/10.1038/364516a0.
- Uenuma, S., Maeda, R., Yokoyama, H., and Ito, K. (2019). Formation of isolated pseudopolyrotaxane nanosheet consisting of α-cyclodextrin and poly (ethylene glycol). Macromolecules 52, 3881–3887. https://doi. org/10.1021/acs.macromol.9b00491.
- Wenz, G., Han, B.H., and Müller, A. (2006). Cyclodextrin rotaxanes and polyrotaxanes. Chem. Rev. 106, 782–817. https://doi.org/10. 1021/cr970027+.
- Liu, W., Johnson, A., and Smith, B.D. (2018). Guest back-folding: a molecular design strategy that produces a deep-red fluorescent host/guest pair with picomolar affinity in water. J. Am. Chem. Soc. 140, 3361–3370. https://doi. org/10.1021/jacs.7b12991.
- Li, S., Taura, D., Hashidzume, A., and Harada, A. (2010). Light-switchable Janus [2]rotaxanes based on alpha-cyclodextrin derivatives bearing two recognition sites linked with oligo(ethylene glycol). Chem. Asian J. 5, 2281– 2289. https://doi.org/10.1002/asia.201000169.
- Katsumata, T., Qu, J., Shiotsuki, M., Satoh, M., Wada, J., Igarashi, J., Mizoguchi, K., and Masuda, T. (2008). Synthesis, characterization, and charge/discharge properties of polynorbornenes carrying 2,2,6,6tetramethylpiperidine-1-oxy radicals at high density. Macromolecules 41, 1175–1183. https://doi.org/10.1021/ma7020425.
- Ceccato, M., Lo Nostro, P., and Baglioni, P. (1997). α-cyclodextrin/polyethylene glycol polyrotaxane: a study of the threading process. Langmuir 13, 2436–2439. https://doi.org/10. 1021/la9609231.





- Zhang, L., Zhang, X., Wu, L., Deng, Y., and Liu, R. (2014). Effect of alkane chain segment length on the crystallization kinetics of nylon 1010, 1013 and 1014. Polym. Int. 63, 1650–1657. https://doi.org/10.1002/pi.4684.
- Yoshikiyo, K., Matsui, Y., and Yamamoto, T. (2012). Determination of binding constants for inclusion complexes of cyclodextrins with organic solvents, ethylene glycol, and its related compounds by means of 1H NMR spectroscopy. Bull. Chem. Soc. Jpn. 85, 1206– 1209. https://doi.org/10.1246/bcsj.20120140.
- Zhang, M.C., Guo, B.-H., and Xu, J. (2017). A review on polymer crystallization theories. Crystals 7 (4). https://doi.org/10.3390/ cryst7010004.
- Li, J., Harada, A., and Kamachi, M. (1994). Solgel transition during inclusion complex formation between α-cyclodextrin and high molecular weight poly (ethylene glycol)s in aqueous solution. Polym. J. 26, 1019–1026. https://doi.org/10.1295/polymj.26.1019.
- Topchieva, I.N., Tonelli, A.E., Panova, I.G., Matuchina, E.V., Kalashnikov, F.A., Gerasimov, V.I., Rusa, C.C., Rusa, M., and Hunt, M.A. (2004). Two-phase channel structures based on alphacyclodextrin-polyethylene glycol inclusion complexes. Langmuir 20, 9036–9043. https:// doi.org/10.1021/la048970d.

- Brown, T., Leonard, G.A., Booth, E.D., and Chambers, J. (1989). Crystal structure and stability of a DNA duplex containing A(anti)-G(syn) base-pairs. J. Mol. Biol. 207, 455–457. https://doi.org/10.1016/0022-2836(89)90268-4.
- de Almeida, A., Nébouy, M., and Baeza, G.P. (2019). Bimodal crystallization kinetics of PBT/ PTHF segmented block copolymers: impact of the chain rigidity. Macromolecules 52, 1227– 1240. https://doi.org/10.1021/acs.macromol. 8b01689.
- Wang, W., Yao, L., Zhang, T., Cheng, C.-Y., Levine, D., and Ishii, H. (2017). Transformative appetite: shape-changing food transforms from 2D to 3D by water interaction through cooking. In Proceedings of the 2017 CHI Conference on Human Factors in Computing Systems, pp. 6123–6132. https://doi.org/10. 1145/3025453.3026019.
- Arazoe, H., Miyajima, D., Akaike, K., Araoka, F., Sato, E., Hikima, T., Kawamoto, M., and Aida, T. (2016). An autonomous actuator driven by fluctuations in ambient humidity. Nat. Mater. 15, 1084–1089. https://doi.org/10.1038/ pmat4693.
- Wang, W., Yao, L., Cheng, C.Y., Zhang, T., Atsumi, H., Wang, L., Wang, G., Anilionyte, O., Steiner, H., Ou, J., et al. (2017). Harnessing the hygroscopic and biofluorescent behaviors of

- genetically tractable microbial cells to design biohybrid wearables. Sci. Adv. 3, e1601984. https://doi.org/10.1126/sciadv.1601984.
- Mu, J., Wang, G., Yan, H., Li, H., Wang, X., Gao, E., Hou, C., Pham, A.T.C., Wu, L., Zhang, Q., et al. (2018). Molecular-channel driven actuator with considerations for multiple configurations and color switching. Nat. Commun. 9, 590. https://doi.org/10.1038/s41467-018-03032-2.
- Domiński, A., Konieczny, T., and Kurcok, P. (2019). α-cyclodextrin-based polypseudorotaxane hydrogels. Materials (Basel) 13, 133. https://doi.org/10.3390/ ma13010133.
- Jeong, B., Bae, Y.H., Lee, D.S., and Kim, S.W. (1997). Biodegradable block copolymers as injectable drug-delivery systems. Nature 388, 860–862. https://doi.org/10.1038/42218.
- Thordarson, P. (2011). Determining association constants from titration experiments in supramolecular chemistry. Chem. Soc. Rev. 40, 1305–1323. https://doi.org/10.1039/ COCS00062K.
- Kline, S.R. (2006). Reduction and analysis of SANS and USANS data using IGOR Pro. J. Appl. Crystallogr. 39, 895–900. https://doi org/10.1107/S0021889806035059.